atmosphere

MDPI

Article

Spatio–Temporal Variation of Extreme Climates and Its Relationship with Teleconnection Patterns in Beijing–Tianjin–Hebei from 1980 to 2019

Jinjie Wang [1] and Anzhou Zhao [2,*]

[1] School of Earth Science and Engineering, Hebei University of Engineering, Handan 056038, China
[2] School of Mining and Geomatics Engineering, Hebei University of Engineering, Handan 056038, China
* Correspondence: zhaoanzhou@hebeu.edu.cn

Abstract: Extreme climate events have a significant impact both on the ecological environment and human society, and it is crucial to analyze the spatial–temporal evolutionary trends of extreme climate. Based on the RClimDex model, this study used trend analysis, probability density function, and wavelet coherence analysis to analyze the spatiotemporal variation characteristics of extreme climate indices and their response mechanisms to teleconnection patterns. The results of the study show that: (1) All the extreme precipitation indices, except max 1-day precipitation amount, max 5-day precipitation amount, and extremely wet days increased, with no significant abrupt changes. The extreme warm indices increased and extreme cold indices decreased. The years with abrupt changes were mainly distributed between 1988 and 1997. (2) Spatially, the extreme precipitation indices of most meteorological stations decreased, except for the simple daily intensity index and the number of very heavy precipitation days. The extreme warm indices of most meteorological stations increased, and the extreme cold indices decreased. (3) Except for consecutive dry days, the frequency of extreme precipitation indices increased significantly, the severity and frequency of high-temperature events increased, while the frequency of low-temperature events increased, but the severity decreased. The results of rescaled range (R/S) analysis indicated that the climate in the Beijing–Tianjin–Hebei region will further tend to be warm and humid in the future. (4) The Polar/Eurasia Pattern, the East Atlantic Pattern, the Arctic Oscillation, and the East Atlantic/West Russian Pattern were most closely associated with extreme climate events in the Beijing–Tianjin–Hebei region. The multi-factor combination greatly enhanced the explanatory power of the teleconnection pattern for extreme climates.

Keywords: extreme climates; teleconnection patterns; spatio–temporal variation; correlation analysis; Beijing–Tianjin–Hebei

Citation: Wang, J.; Zhao, A. Spatio–Temporal Variation of Extreme Climates and Its Relationship with Teleconnection Patterns in Beijing–Tianjin–Hebei from 1980 to 2019. *Atmosphere* **2022**, *13*, 1979. https://doi.org/10.3390/atmos13121979

Academic Editors: Elenio Avolio and Nicola Scafetta

Received: 3 October 2022
Accepted: 24 November 2022
Published: 27 November 2022

1. Introduction

Global climate change is one of the biggest and most complex challenges of our times [1–3]. Global warming has increased the frequency and intensity of extreme climate events since the 20th century, which has had a serious impact on the ecological environment, the economy, and society [4–8]. The Intergovernmental Panel on Climate Change (IPCC) Sixth Assessment Report [9] has also pointed out the evidence of observed changes in extreme events such as heavy rainfall, heat waves, and high temperatures. The likelihood of these events has increased over the last 50 years due to global warming; therefore, assessing the change in extreme climate events has become one of the widely discussed issues globally.

A number of scholars have analyzed extreme climate events on both local and global scales. Alexander et al. [10], Diffenbaugh et al. [11], and Yuan et al. [12] have analyzed the changes on a global scale and pointed out that extreme climate events have changed significantly with an increasing warming and wetting trend. On a regional scale, the

studies [13,14] have found an increase in wet days and a decrease in dry days in West Africa, which has led to an increase in overall humidity levels in the atmosphere. In Indonesia, the extreme temperature indices showed an increasing trend, while the change in extreme precipitation indices did not vary significantly and the climate tended to be warm and humid [15]. Australia's extreme temperature events have increased significantly in the 21st century, but the change in extreme precipitation events was observed to be insignificant, and the climate tends to be warm and dry [16].

The study of extreme climate events in China has increased recently. Han et al. showed that extreme precipitation events have followed an increasing trend throughout mainland China, and the increase is much more pronounced in arid areas [17]. According to Guo et al. [18], extreme warm indices in northeast China have increased, while extreme cold indices and extreme precipitation indices have decreased, excluding consecutive dry days (CDD). Based on the regional model (RegCM4), Wu et al. simulated extreme climate changes in ten river basins in China under the global warming scenario of 1.5–4 °C and the results projected an increase in warm and wetness indices [7].

Changes in extreme climate are constrained by many factors [19–21]. Atmospheric circulation factors, mainly through the form of teleconnection, are the main constraints of extreme climate change [22,23]. Many scholars have explored the response relationship between extreme climate events and teleconnection patterns, thus providing a more comprehensive understanding of extreme climate events [23–32]. However, it should be noted that the changes in extreme climate events are very complex; their occurrence patterns and influencing mechanisms are not yet completely clear [33].

The "Plan of Beijing-Tianjin-Hebei Collaborative Development" clearly pointed out that the ecological environment is the foundation of the integrated coordinated development of Beijing–Tianjin–Hebei, and it was suggested to build the ecological system of the Beijing–Tianjin–Hebei city cluster. The Beijing–Tianjin–Hebei cluster, the capital circle of China, has experienced an increase in the frequency of extreme climate events since 1980s, with high temperatures and drought disasters affecting the crop phenological seasons and ecological environment of the region [34]. Some studies have analyzed extreme climate events in this region. Zhao et al. [35], and Wang et al. [36] pointed out that extreme heat events increased in the Beijing–Tianjin–Hebei region during 1961–2018, and that the size and location of a city determined its contribution to extreme heat. Tong et al. [37] analyzed the climate extremes in the Beijing–Tianjin–Hebei region from 1959 to 2018 and found that the climate tends to be warm and dry, while the East Asian summer monsoon and rapid urbanization may be the main influencing factors. Song et al. [38] showed that precipitation extremes oscillated significantly in the Beijing–Tianjin–Hebei region during 1958–2017, and were strongly correlated with ENSO, IOD, and NAO. Overall, the previous studies either selected a single extreme climate index or a limited number of influencing factors, and the research on the response relationship between extreme climate and teleconnection patterns is also limited.

In this paper, we calculated the extreme climate indices (nine extreme temperature indices and nine extreme precipitation indices) of the Beijing–Tianjin–Hebei region based on the RClimDex model, comprehensively analyzed the spatio–temporal variation characteristics and their response mechanisms to nine teleconnection patterns at locations such as middle and high latitudes in the northern hemisphere using trend analysis, the Pettitt mutation test, the probability density function, rescaled range analysis (R/S), correlation analysis, and wavelet coherence analysis to provide a theoretical basis for local disaster reduction and prevention work.

2. Data and Methods

2.1. Study Area

The Beijing–Tianjin–Hebei region is located to the north of the North China Plain (NCP), between 113°27′ E–119°50′ E, 36°03′ N–42°40′ N. In addition, the region is located west of the Bohai Sea, east of the Taihang Mountains, and south of the Yan Mountains,

including Beijing, Tianjin, and Hebei Province, with a total area of about 2.18 × 10^5 km^2 (Figure 1). The climate of the region falls within the temperate semi-humid and semi-arid continental climates, characterized by dry windy springs, hot wet summers, and cold dry winters [35,39]. The average annual temperature of this region is 10–11 °C, while the variation in annual precipitation ranges between 400 and 800 mm, with four distinct seasons. During recent decades, particularly in the years experiencing significantly increased temperatures, extreme weather and climate events (e.g., extreme precipitation, frozen rain, and droughts) have also become frequent in this region.

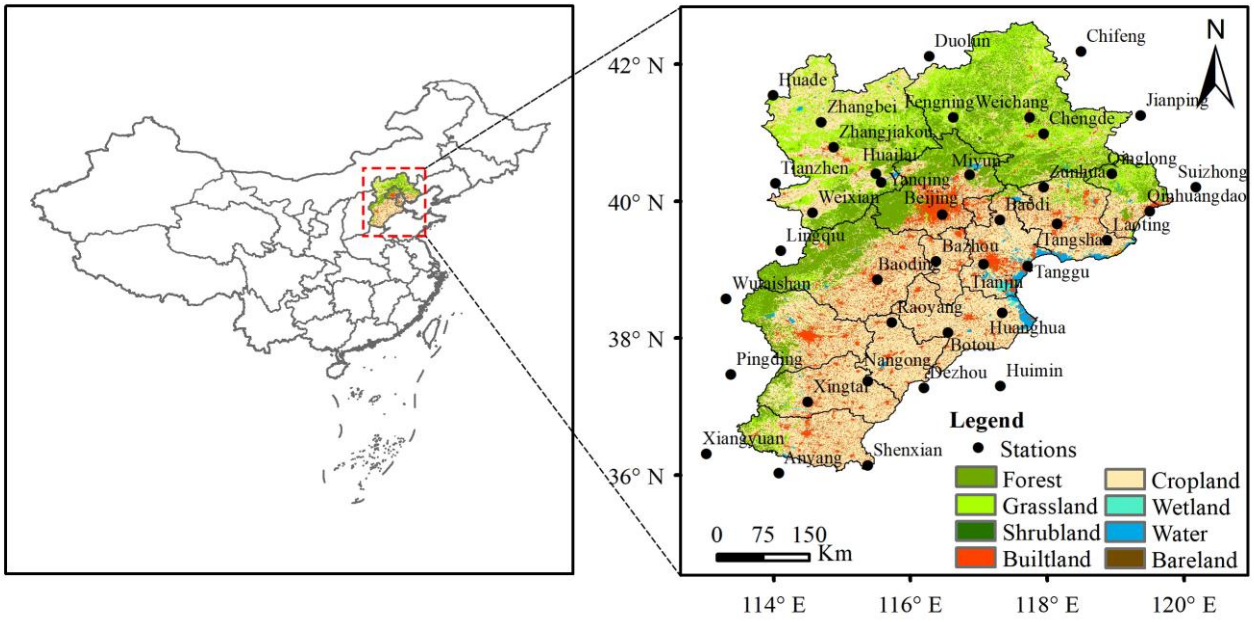

Figure 1. The location of the Beijing–Tianjin–Hebei region of China.

2.2. Data Source and Processing

Meteorological data were obtained from the China Meteorological Data Network (http://data.cma.cn/, accessed on 21 February 2022), including daily maximum temperature, daily minimum temperature, and daily precipitation data from 39 meteorological stations (25 in the Beijing–Tianjin–Hebei region, and 14 in surrounding areas) from 1980 to 2019. The meteorological data have a total of 1608 data missing. Studies have shown that the linear interpolation method can effectively estimate meteorological data [40,41]. Therefore, the linear interpolation method was used to interpolate missing data to ensure the continuity and integrity of the meteorological data. The data of monthly teleconnection indices for the period 1980-2019 were obtained from the Climate Prediction Center (https://www.cpc.ncep.noaa.gov/, accessed on 12 February 2022), including the East Atlantic Pattern (EA), the East Atlantic/West Russian Pattern (EAWR), the North Atlantic Oscillation (NAO), the Pacific North American Pattern (PNA), the Polar/Eurasia Pattern (PolarEA), the Scandinavian Pattern (SCAND), the Western Pacific Pattern (WP), the El Nino–Southern Oscillation (ENSO 3.4), and the Arctic Oscillation (AO), which affect global and regional climate [42]. Land cover data for the Beijing–Tianjin–Hebei region in 2020 were sourced from the Global Land Cover Data Product Service website of the National Basic Geographic Information Center (DOI: 10.11769, accessed on 28 May 2022), with a spatial resolution of 30 m.

2.3. Methods

2.3.1. Selection of Extreme Climate Indices

The RClimDex model is an R-based editor developed by the Canadian Research Centre that uses daily maximum temperature, daily minimum temperature, and daily precipitation data to compute the 27 core indices of extreme climate (16 extreme temperature indices and

11 extreme precipitation indices) [43]. This paper used the RClimDex model to check and control the data quality of the selected meteorological stations, including whether the daily precipitation was greater than 0, whether the daily minimum temperature was greater than the daily maximum temperature, and outlier testing, etc. Due to the excessive number of indices and the close relationship between each other, 18 representative indices (9 extreme temperature indices and 9 extreme precipitation indices) were selected using the Principal Component Analysis Method (PCA) for subsequent research (Table 1).

Table 1. Selection of extreme climate indices in this study.

	Type	ID	Indicator Name	Definition	Unit
Extreme Precipitation Indices	Intensity indices	RX1day	Max 1-day precipitation amount	Monthly maximum 1-day precipitation	mm
		RX5day	Max 5-day precipitation amount	Monthly maximum consecutive 5-day precipitation	mm
		SDII	Simple daily intensity index	Annual total precipitation divided by the number of wet days (defined as PRCP >= 1.0 mm) in the year	mm/d
	Relative indices	R95P	Very wet days	Annual total PRCP when RR > 95th percentile	mm
		R99P	Extremely wet days	Annual total PRCP when RR > 99th percentile	mm
	Absolute indices	R20mm	Number of very heavy precipitation days	Annual count of days when PRCP >= 20 mm	d
		R25mm	Number of extreme precipitation days	Number of days with PRCP >= 25 mm	d
	Duration indices	PRCPTOT	Annual total wet-day precipitation	Annual total PRCP in wet days (RR >= 1 mm)	mm
		CDD	Consecutive dry days	Maximum number of consecutive days with RR < 1 mm	d
Extreme Temperature Indices	Absolute indices	FD0	Frost days	Annual count when TN(daily minimum) < 0 °C	d
	Extreme-value indices	TXn	Min Tmax	Monthly minimum value of daily maximum temp	°C
		TNn	Min Tmin	Monthly minimum value of daily minimum temp	°C
	Relative indices	TX10P	Cool days	Percentage of days when TX < 10th percentile	d
		TN10P	Cool nights	Percentage of days when TN < 10th percentile	d
		TX90P	Warm days	Percentage of days when TX > 90th percentile	d
		TN90P	Warm nights	Percentage of days when TN > 90th percentile	d
	Other indices	DTR	Diurnal temperature range	Monthly mean difference between TX and TN	°C
		GSL	Growing season length	Annual (1st Jan to 31st Dec in NH, 1st July to 30th June in SH) count between first span of at least 6 days with TG > 5 °C and first span after July 1 (January 1 in SH) of 6 days with TG < 5 °C	d

PRCP is an abbreviation of precipitation; RR is an abbreviation of daily precipitation.

2.3.2. Principal Component Analysis Method (PCA)

The principal component analysis method is a multivariate statistical analysis method that transforms multiple original variables into a few unrelated important variables through linear transformation [44]. It can reduce and simplify the original data on the premise of retaining the important information of variables [44–46]. The main principles are:

Assume that the original variable is $x_1, x_2, \ldots, x_j$, and the new variable obtained after PCA is $z_1, z_2, \ldots, z_m$, $(m < j)$. First, standardize the original data, obtaining the standardized matrix X:

$$y_{ij} = \left(x_{ij} - \bar{x}_j\right)/S_j, \left(i = 1, 2, \cdots I; j = 1, 2, \cdots J\right) \quad (1)$$

where $\bar{x_j}$ and S_j are the sample mean and sample standard deviation of the n-th index, respectively.

Calculate the correlation matrix R, and then calculate J eigenvalues λ_J ($\lambda_1 \geq \lambda_2 \geq \cdots \geq \lambda_J$), and eigenvector $a_1, a_2, \cdots, a_J$ of R.

Calculate contribution rate (e_J) and cumulative contribution rate (E_k):

$$e_J = \lambda_J / \sum_{k=1}^{m} \lambda_k \tag{2}$$

$$E_k = \sum_{k=1}^{m} \lambda_k / \sum_{j=1}^{J} \lambda_j \tag{3}$$

Calculate the principal component:

$$z_k = \sum_{j=1}^{J} a_j x_j, \ (j = 1, 2, \cdots J; k = 1, 2, \cdots J) \tag{4}$$

Generally, we select the first $m (m < j)$ principal components corresponding to the eigenvalues whose cumulative contribution rate is greater than 80%.

2.3.3. Trend Analysis

Sen's slope estimator is a robust nonparametric statistical method. When compared with the linear trend of least square fitting, Sen's slope estimator, which is often used in trend analysis of long time series data, can avoid data loss in time series and eliminate the effect of outliers [18,47] (Equation (5)).

$$Sen = Median\left(\frac{x_j - x_i}{j - i}\right) \tag{5}$$

where Sen is the trend of extreme climate indices; i and j are time series, respectively; x_i and x_j represent the value of extreme climate index at the time i and j. When $Sen > 0$, the extreme climate index shows an increasing trend and vice versa.

The Mann–Kendall (M-K) test was used to test the significance of increasing or decreasing trends of extreme climate indices [48]. When the test statistic (MMK) was greater than 1.96 in absolute value, it was considered significant based on the 95% significance level test.

2.3.4. Pettitt Mutation Test

The Pettitt mutation test method, a non-parametric test method, is widely used in time series mutation point testing [49]. For climate series x with a sample size of n, a statistical test was constructed (Equation (6)).

$$S_k = 2\sum_{i=1}^{k} r_i - k(n+1), \ k = 1, \ldots, n \tag{6}$$

where r_i is the rank at time i, and k is the length of the time series. If significant mutations occur in year t, then:

$$S_t = \max_{1 \leq t \leq n} |S_k|, |S_t| \geq S_\alpha \tag{7}$$

where S_α is the critical Pettitt test value of the corresponding sample number.

2.3.5. Rescaled Range (R/S) Analysis

In this study, rescaled range (R/S) analysis was used to continuously predict the change in trend of extreme climate indices in Beijing–Tianjin–Hebei. Rescaled range analysis is a non-parametric statistical method proposed by British scientist Hurst, which

uses the Hurst index to quantitatively describe the continuity of time series [50]. The main principles are:

For a time series $x_1, x_2, \ldots, x_n$ (n is the length of the time series), for any positive integer $f \geq 1$, the mean sequence is:

$$\bar{x_f} = \frac{1}{f}\sum_{i=1}^{n} x_i, (f = 1,\ 2,\ \cdots, n) \tag{8}$$

Cumulative deviation:

$$X(t, f) = \sum_{u=1}^{t}\left(x_\mu - \bar{x_f}\right), \qquad (1 \leq t \leq f) \tag{9}$$

Range:

$$R(f) = \max_{1\leq t\leq f} X(t, f) - \min_{1\leq t\leq f} X(t, f) \tag{10}$$

Standard deviation:

$$S(f) = \left[\frac{1}{f}\sum_{\mu=1}^{f}\left(x_\mu - \bar{x_f}\right)^2\right]^{\frac{1}{2}} \tag{11}$$

Then, the following relationship was defined in Equation (12):

$$\frac{R(f)}{S(f)} = (cf)^H \tag{12}$$

where c is a constant and H is the Hurst index of the time series, taking values in the range (0, 1). When H = 0.5, the time series is completely independent and the future changes are random; when $0 < H < 0.5$, the time series shows anti-continuity, the overall trend of future changes is opposite to that of the past, and the closer H is to 0, the stronger the anti-continuity is; when $0.5 < H < 1$, the time series has continuity, the trend of future changes is consistent with the past, and the closer H is to 1, the stronger the continuity is.

2.3.6. Correlation Analysis

The Pearson correlation coefficient method was used to analyze the correlation between extreme climate events and teleconnection patterns and *t*-test was used to calculate the significance of the correlation coefficient.

In addition, the correlation between extreme climate events and teleconnection patterns in time and frequency space was further analyzed using wavelet transform coherence (WTC) and multiple wavelet coherence (MWC). The significance level of the correlation was determined by Monte Carlo methods [51,52]. Given time series X and Y, the WTC (Equation (13)) was defined by Torrence and Webster [53], and Grinsted et al. [51] as follows:

$$R_n^2(S) = \frac{\left|S\left(s^{-1}W_n^{XY}(s)\right)\right|^2}{\left|S(s^{-1}|W_n^X(s)|)\right|^2 - \left|S(s^{-1}|W_n^Y(s)|)\right|^2} \tag{13}$$

where S is a smoothing operator defined as:

$$W_i^{XY}(s) = W_i^X(s) \cdot W_i^Y * (s) \tag{14}$$

where s is the wavelet scale; * denotes the complex conjugate. Wavelet transform coherence takes values in the range [0, 1], with 0 indicating that the two series are uncorrelated and 1 indicating that they are fully correlated.

Multiple wavelet coherence can extend wavelet coherence from two variables to multiple variables. Given a predictor variable set X (X = {$X1$, $X2$, . . . , Xq}) and a response variable Y, the MWC (Equation (15)) was defined as follows [51,53,54]:

$$\rho_m^2(s,\tau) = \frac{\overleftrightarrow{w}^{Y,X}(s,\tau)\overleftrightarrow{w}^{X,X}(s,\tau)^{-1}\overleftrightarrow{w}^{Y,X}(s,\tau)^*}{\overleftrightarrow{w}^{Y,Y}(s,\tau)} \quad (15)$$

where $\overleftrightarrow{w}^{Y,X}(s,\tau)$ is the smoothed cross-wavelet power spectra between Y and X; $\overleftrightarrow{w}^{X,X}(s,\tau)$ is the smoothed auto- and cross-wavelet power spectra among X; $\overleftrightarrow{w}^{Y,Y}(s,\tau)$ is the smoothed wavelet power spectrum of Y; and $\overleftrightarrow{w}^{Y,X}(s,\tau)^*$ is the complex conjugate of $\overleftrightarrow{w}^{Y,X}(s,\tau)$.

The 95% significance level of the WTC and MWC were calculated using Monte Carlo method [51,54].

3. Results

3.1. Spatial–Temporal Variation Characteristics of Extreme Climates

3.1.1. Spatial–Temporal Variation of Extreme Precipitation Indices

The variation trend of the extreme precipitation indices in Beijing–Tianjin–Hebei for the period 1980-2019 is shown in Figure 2. There was an increasing trend observed in PRCPTOT (0.83 mm·a^{-1}), R95P (0.27 mm·a^{-1}), CDD (0.26 d·a^{-1}), R20mm (0.02 d·a^{-1}), R25mm (0.02 d·a^{-1}), and SDII (0.02 mm/d·a), but their effect was non-significant at a 95% confidence level (Figure 2a). Only three variables, R99P, RX1day, and RX5day, showed a decreasing trend at a rate of −0.26 mm·a^{-1}, −0.07 mm·a^{-1}, and −0.03 mm·a^{-1}, respectively, which were also non-significant. There were also no significant abrupt changes in the extreme precipitation indices in the Beijing–Tianjin–Hebei region (Figure 2b) for the period 1980 to 2019.

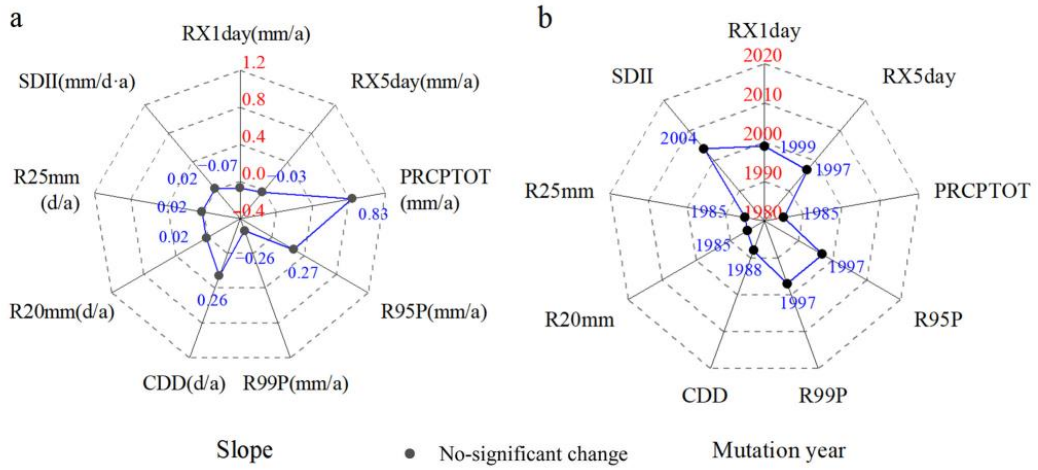

Figure 2. Trends (**a**) and abrupt years (**b**) of extreme precipitation indices in the Beijing–Tianjin–Hebei region from 1980 to 2019 (confidence level 95%).

The spatial pattern of extreme precipitation indices across Beijing–Tianjin–Hebei for the period 1980–2019 is shown in Figure 3. All of the extreme precipitation indices, except CDD, showed an increasing trend from northwest to southeast. The detailed information of the extreme precipitation index at each station is shown in Table 2.

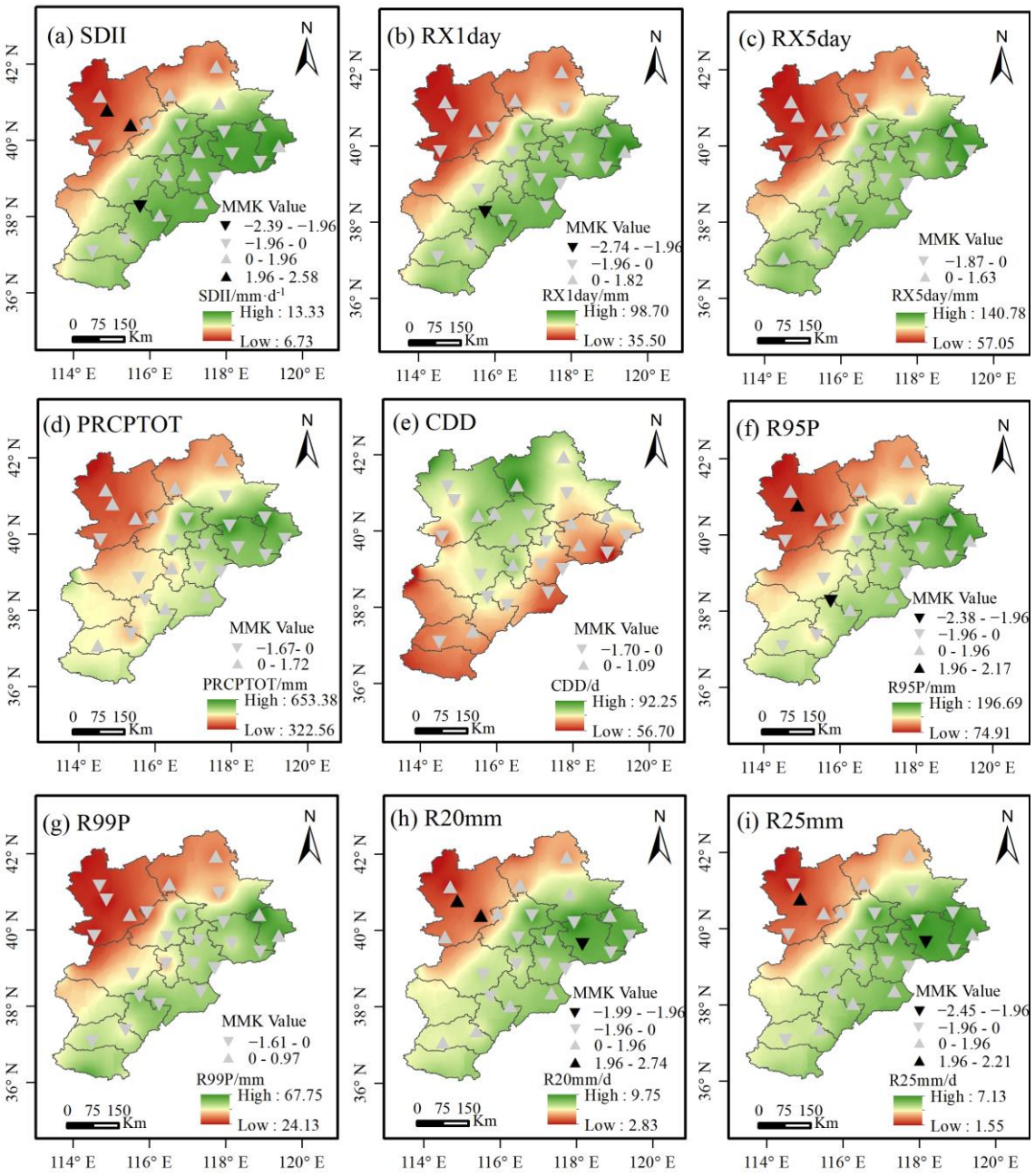

Figure 3. Spatial distribution of averaged extreme precipitation indices and trends in Beijing–Tianjin–Hebei during 1980–2019 (|MMK| > 1.96 means passing 95% confidence level); (**a**) SDII; (**b**) RX1day; (**c**) RX5day; (**d**) PRCPTOT; (**e**) CDD; (**f**) R95P; (**g**) R99P; (**h**) R20mm; (**i**) R25mm.

For the intensity indices (Figure 3a–c), the SDII of 60% (15/25) of the meteorological stations showed an increasing trend, among which the stations passing the 95% significance test were mainly concentrated in the northwest Hauts Plateau and the central region. RX1day, and RX5day decreased in most regions, accounting for 76% (19/25) and 60% (15/25) of Beijing–Tianjin–Hebei stations, respectively. Only one station in the central region had a downward trend of RX1day, and its effect was found to be significant at a 95% significance test.

Table 2. Extreme precipitation indices at 25 meteorological stations in the Beijing–Tianjin–Hebei region from 1980 to 2019.

Stations	RX1day (mm)	RX5day (mm)	SDII (mm/d)	R95P (mm)	R99P (mm)	R20mm (d)	R25mm (d)	PRCPTOT (mm)	CDD (d)
Zhangbei	37.82	60.00	7.20	84.41	26.67	3.28	1.80	373.66	79.30
Weixian	38.67	58.42	7.56	88.93	24.51	4.45	2.73	393.74	68.60
Xingtai	79.61	125.82	11.29	145.27	50.80	6.55	4.80	492.88	71.33
Fengning	47.57	74.84	8.67	105.41	30.52	5.18	3.40	440.55	91.95
Weichang	46.31	74.74	8.09	107.70	32.76	5.00	3.48	431.36	76.85
Zhangjiakou	39.01	60.42	7.71	88.21	24.32	4.33	2.63	386.26	75.25
Huailai	41.48	59.89	8.04	83.84	26.05	4.18	2.38	373.53	85.35
Yanqing	48.16	74.06	8.99	102.15	30.91	5.48	3.50	432.47	82.78
Miyun	87.09	129.44	12.52	179.39	56.78	8.98	6.78	617.43	83.00
Chengde	54.45	88.26	9.91	122.28	35.81	6.93	4.80	493.29	75.75
Zunhua	85.31	127.75	12.91	182.76	54.69	9.75	7.13	653.39	73.68
Qinglong	90.31	140.78	12.68	196.70	67.75	9.00	6.93	651.96	77.63
Qinhuangdao	98.70	138.81	13.33	183.61	61.79	8.90	6.83	604.53	72.78
Beijing	73.19	114.26	11.83	145.78	48.42	8.00	5.80	525.94	81.85
Bazhou	72.96	107.32	11.50	135.11	39.41	6.60	5.00	468.86	84.68
Baodi	81.17	121.56	12.53	153.47	51.52	8.33	6.40	553.77	78.93
Tianjin	85.68	114.24	11.99	153.04	50.40	7.35	5.43	510.46	74.05
Tangshan	75.77	111.18	12.78	156.37	47.78	8.60	6.80	572.61	71.20
Laoting	88.22	128.91	12.86	173.63	54.93	8.40	6.53	573.96	63.53
Baoding	68.87	101.46	11.40	131.95	42.81	7.23	5.38	485.88	79.38
Raoyang	84.65	117.46	11.80	147.42	56.61	7.05	5.08	484.75	79.23
Botou	90.05	126.11	12.56	162.10	56.70	7.55	5.65	520.00	75.75
Tanggu	88.76	122.90	12.47	165.39	56.62	7.55	5.78	537.75	68.30
Huanghua	85.22	119.91	12.35	158.92	52.45	7.85	5.98	541.53	68.40
Nangong	70.23	104.14	10.77	128.03	44.43	6.48	4.78	450.78	73.35

For the duration indices (Figure 3d,e), 60% (15/25) and 52% (13/25) of the stations showed a downward trend for PRCPTOT and CDD, respectively, and the effect of this trend was found to be non-significant.

For the relative indices (Figure 3f,g), R95P showed a downward trend at 52% (13/25) of the meteorological stations. The stations with the significant downward trend were mainly concentrated in the northwest Hauts Plat and the central region. R99P also showed a downward trend at 76% (19/25) of the meteorological stations, and the trend was found to be non-significant at all stations.

For the absolute indices (Figure 3h,i), 56% (14/25) of the meteorological stations showed an increasing trend for R20mm, while 60% (15/25) showed a decreasing trend for R25mm. The stations with a significant increasing trend were mainly concentrated on the northwest Hauts Plateau, and those with a significant decreasing trend were distributed in the eastern coastal area.

3.1.2. Spatial–Temporal Variation of Extreme Temperature Indices

The variation trend of the extreme temperature indices in Beijing–Tianjin–Hebei for the period 1980–2019 is shown in Figure 4. The extreme temperature indices (GSL, TXn, TNn, TN90P, and TX90P) representing the occurrence of warm events showed an increasing trend, with GSL, TN90P, and TX90P increasing significantly at a rate of 0.32 $d \cdot a^{-1}$, 0.3 $d \cdot a^{-1}$, and 0.24 $d \cdot a^{-1}$, respectively. The temperature indices (FD0, TN10P, TX10P, and DTR), representing the occurrence of cold events, showed a decreasing trend, with FD0, TN10P, and TX10P decreasing significantly at the rate of -0.35 $d \cdot a^{-1}$, -0.25 $d \cdot a^{-1}$, and -0.17 $d \cdot a^{-1}$, respectively. In addition, the growth rates of TN90P and TX90P were greater than TN10P and TX10P, respectively, indicating that the climate tended to be warm across the Beijing–Tianjin–Hebei region. The years with abrupt changes in extreme temperature indices were mainly distributed in the period 1988–1997, and the abrupt changes in TXn, TNn, DTR, and TX10P were not significant (Figure 4b).

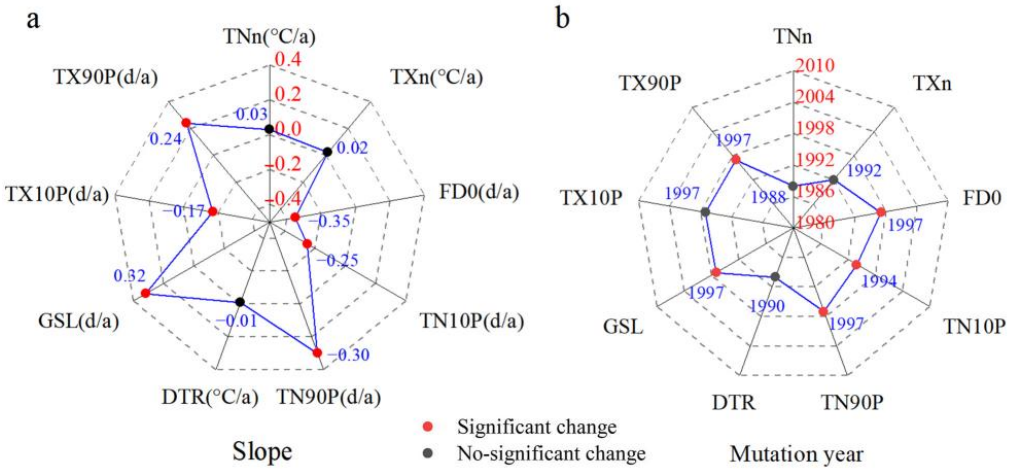

Figure 4. Trends (**a**) and abrupt years (**b**) of extreme temperature indices in the Beijing–Tianjin–Hebei region from 1980 to 2019 (confidence level 95%).

Figure 5 shows the spatial pattern of extreme temperature indices across Beijing–Tianjin–Hebei during 1980–2019. The detailed information of the extreme temperature index at each station is shown in Table 3.

Table 3. Extreme temperature indices at 25 meteorological stations in the Beijing–Tianjin–Hebei region from 1980 to 2019.

Stations	FD0 (d)	TXn (°C)	TNn (°C)	TX10P (d)	TN10P (d)	TX90P (d)	TN90P (d)	DTR (°C)	GSL (d)
Zhangbei	189.53	−18.80	−29.78	13.92	13.63	13.68	13.66	12.34	188.43
Weixian	161.23	−12.01	−25.13	13.74	13.93	13.60	13.77	13.55	219.70
Xingtai	86.73	−3.21	−10.62	13.90	13.70	13.80	13.75	9.86	275.18
Fengning	171.95	−12.59	−23.61	13.67	13.65	13.89	13.55	13.88	214.85
Weichang	180.10	−15.58	−24.93	13.81	13.74	13.77	13.67	13.01	202.88
Zhangjiakou	143.38	−11.64	−20.27	13.88	13.77	13.74	13.64	11.59	227.70
Huailai	139.90	−9.96	−18.51	13.74	13.76	13.63	13.69	11.84	233.70
Yanqing	147.63	−9.03	−20.68	13.85	13.76	13.88	13.67	12.38	229.90
Miyun	135.30	−5.91	-18.18	13.78	13.68	13.70	13.61	12.32	241.75
Chengde	151.90	−9.79	−21.10	13.82	13.76	13.70	13.75	13.16	227.00
Zunhua	128.50	−5.96	−17.30	13.87	13.88	13.83	13.63	11.55	244.60
Qinglong	146.03	−7.99	−20.72	13.80	13.68	13.83	13.70	12.61	231.63
Qinhuangdao	122.98	−6.72	−16.21	13.68	13.73	13.81	13.63	9.16	240.15
Beijing	112.25	−4.97	−13.26	13.84	13.65	13.68	13.68	10.28	254.95
Bazhou	117.03	−4.69	−15.53	13.71	13.82	13.73	13.67	11.18	252.70
Baodi	126.78	−5.68	−16.16	13.94	13.67	13.72	13.64	11.50	244.60
Tianjin	107.50	−5.02	−13.61	13.92	13.56	13.64	13.71	9.93	255.35
Tangshan	123.58	−6.22	−17.16	13.89	13.66	13.67	13.62	11.02	245.25
Laoting	121.63	−6.49	−16.05	13.96	13.85	13.84	13.75	10.02	244.65
Baoding	106.55	−4.28	−13.56	13.78	13.73	13.83	13.75	10.54	259.83
Raoyang	113.58	−4.39	−15.31	13.75	13.63	13.78	13.70	11.37	258.33
Botou	107.40	−4.41	−14.58	13.76	13.68	13.75	13.80	10.77	260.50
Tanggu	97.48	−5.55	−12.48	13.80	13.72	13.76	13.58	7.76	254.63
Huanghua	108.08	−5.00	−13.95	13.73	13.77	13.67	13.68	10.20	255.95
Nangong	107.03	−3.73	−14.24	13.78	13.62	13.80	13.67	11.34	263.48

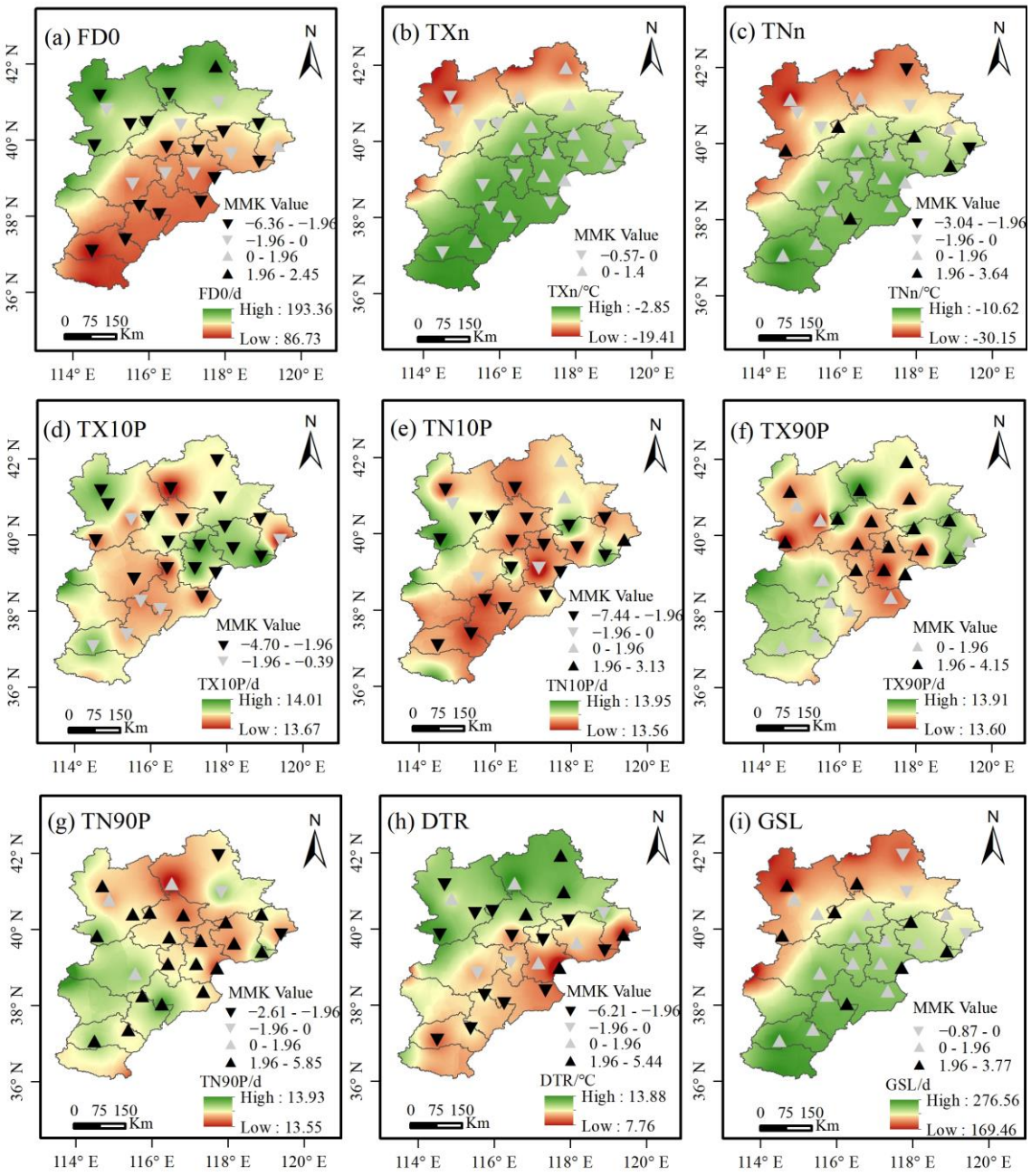

Figure 5. Spatial distribution of averaged extreme temperature indices and trends in Beijing–Tianjin–Hebei during 1980–2019 (|MMK| >1.96 means passing 95% confidence level); (**a**) FD0; (**b**) TXn; (**c**) TNn; (**d**) TX10P; (**e**) TN10P; (**f**) TX90P; (**g**) TN90P; (**h**) DTR; (**i**) GSL.

For the absolute indices (Figure 5a), the regional average of FD0 decreased from northwest to southeast, and 88% (22/25) of the meteorological stations showed a downward trend, of which 64% (16/25) showed a significant downward trend; the stations that did not pass the 95% significance test were mainly concentrated in the central area of Beijing–Tianjin–Hebei.

For the extreme value indices (Figure 5b,c), the regional averages of TXn and TNn both increased from northwest to southeast. The TXn of 56% (14/25) of the meteorological stations showed an increasing trend, with no station passing the 95% significance test. A total of 68% (17/25) of stations showed an increasing trend of TNn, of which 20% (5/25) showed a significant increase, mainly in the northern and central parts of Beijing–ng–Tianjin–Hebei.

For the relative indices (Figure 5d–g), the highest regional values of TX10P and TN10P were mainly distributed in the western, southern, and eastern coastal areas of Beijing–Tianjin–Hebei. The TX10P of all the meteorological stations and the TN10P of 88% (22/25) showed a downward trend, among which 76% (19/25) showed a significant downward trend, concentrated in the north and southeast of Beijing–Tianjin–Hebei. The highest values of TX90P and TN90P were mainly distributed in the central–southern and northern regions of Beijing–Tianjin–Hebei. The TX90P of all the meteorological stations and the TN90P of 88% (22/25) showed an increasing trend, among which 64% (16/25) and 76% (19/25) showed a significant increasing trend, respectively, concentrated in the northern and southeastern regions of Beijing–Tianjin–Hebei.

For other indices (Figure 5h,i), the regional average GSL increased from northwest to southeast; 88% (22/25) of the meteorological stations showed an increasing trend, of which 32% (8/25) passed the 95% significance test, mainly concentrated in the northwest plateau and eastern coastal areas. The regional average of DTR decreased from northwest to southeast. A total of 64% (16/25) of the stations showed a downward trend, of which 52% (13/25) showed a significant downward trend, mainly concentrated in the northwest plateau and southeast coastal areas.

3.2. Analysis of Future Trends

3.2.1. Probability Density Function of Extreme Climate Indices

Changes in the frequency and intensity of extreme climate are also important indicators reflecting trends of extreme climate change [21]. Since RX1day was the latest to have a sudden change in 1999, all indices were divided into two time periods: 1980–1999, and 2000–2019, to further analyze the trends of the temporal variation of the extreme climate indices. The probability of the occurrence of indices based on the probability density function was analyzed for these specified time periods.

The probability density function of the extreme precipitation indices in the Beijing–Tianjin–Hebei region for the period 1980–2019 is shown in Figure 6. The results showed that the frequency of all the indices except CDD increased significantly, in which RX1day, RX5day, R95P, and R99P moved to the left from the first (1980–1999) to the second (2000–2019) period, indicating a decrease in the severity but an increase in the frequency of extreme precipitation events. Consecutive dry days moved to the left from the first (1980–1999) to the second (2000–2019) period, but its frequency decreased, indicating a decrease in the severity and frequency of drying events in the Beijing–Tianjin–Hebei region. The Kolmogorov–Smirnov (K-S) test results showed that all indexes had significant differences in pdf distribution between the two periods, except RX1day and RX5day. The increase in the probability of extreme rainfall events in Beijing–Tianjin–Hebei in the future may lead to an increase in floods.

The probability density function of the extreme temperature indices in Beijing–Tianjin–Hebei for the period 1980 to 2019 is shown in Figure 7. For absolute indices, FD0 moved to the left from the first (1980–1999) to the second (2000–2019) period; its severity decreased and frequency increased. For the extreme value indices, the positions of the TXn and TNn curves in both the time periods roughly coincided, but the frequency of the moderate extreme temperature events increased. For the relative indices, both TX10P and TN10P moved to the left from the first (1980–1999) to the second (2000–2019) period, with a significant decrease in severity and an increase in the frequency of occurrence. TX90P and TN90P moved to the right from the first (1980–1999) to the second (2000–2019) period, with an increase in severity and a decrease in the frequency of occurrence. For other indices, GSL moved to the right from the first (1980–1999) to the second (2000–2019) period, with an increase in both severity and frequency, while DTR moved to the left from the first (1980–1999) to the second (2000–2019) period, with a decrease in severity and a significant increase in frequency. The Kolmogorov–Smirnov test (K-S) results showed that the pdf distribution of TNn, TX10P, TN10P, and DTR differed significantly in the two periods.

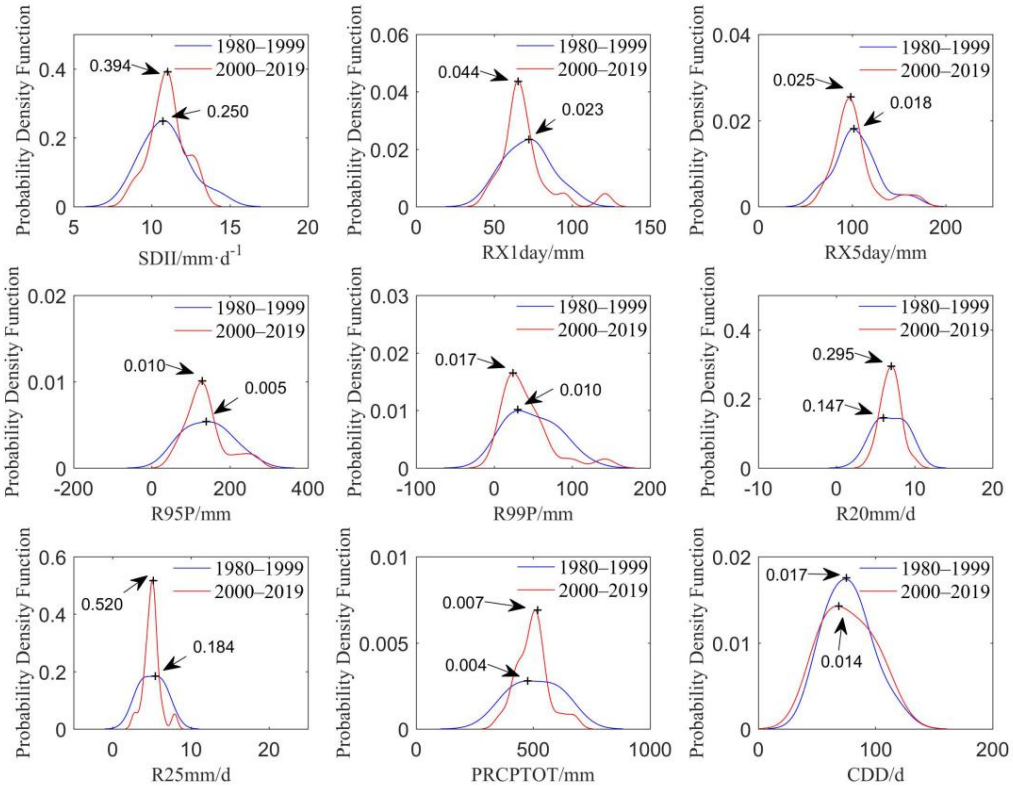

Figure 6. Probability density functions for Beijing–Tianjin–Hebei extreme precipitation indices from 1980 to 2019 for two time periods: 1980–1999, and 2000–2019.

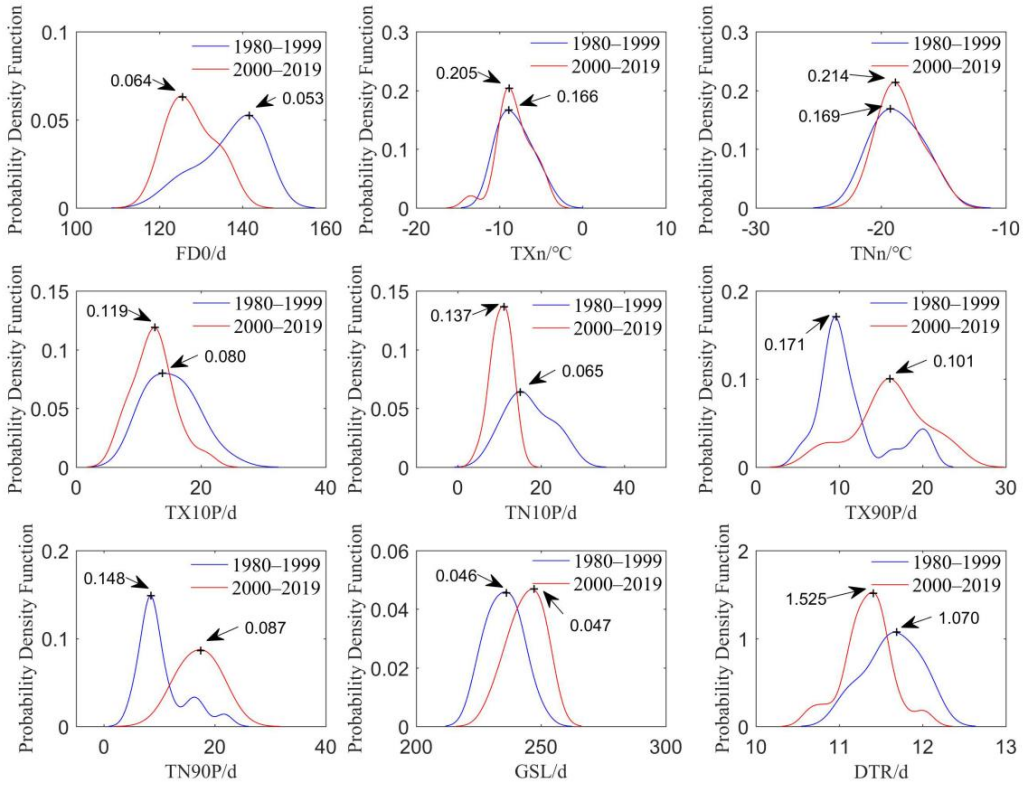

Figure 7. Probability density functions for Beijing–Tianjin–Hebei extreme temperature indices from 1980 to 2019 for two time periods: 1980–1999, and 2000–2019.

3.2.2. Continuous Prediction of Extreme Climate Indices

Further in this study, a continuous prediction of extreme climate indices for the period 1980 to 2019 (Table 4) was generated by R/S analysis to further understand the development trend of extreme climate events in the Beijing–Tianjin–Hebei region. In terms of extreme precipitation indices, the results showed a weak continuity in the trends of RX5day, R20mm, R25mm, SDII, and PRCPTOT, among which R20mm (0.6258) exhibited the strongest continuity, indicating that the past trend of these indices will be continued in the future. All the other indices showed anti-continuity, among which CDD (0.1496) showed the highest intensity of anti-continuity, indicating that RX1Day and R99P will increase in the future, while R95P and CDD will decline. As for the extreme temperature indices, all trends showed continuity, among which TN10P was the strongest and TXn the weakest, indicating that the pattern of extreme temperature indices in the Beijing–Tianjin–Hebei region will maintain the past 40 year trend in the future.

Table 4. Hurst index of Beijing–Tianjin–Hebei extreme climate indices.

Precipitation Indices	**RX1day**	**RX5day**	**R95P**	**R99P**	**R20mm**	**R25mm**	**CDD**	**SDII**	**PRCPTOT**
Hurst	0.4356	0.5312	0.4511	0.4302	0.6258	0.5512	0.1496	0.5543	0.5485
Temperature indices	**FD0**	**GSL**	**TXn**	**TNn**	**TN10P**	**TN90P**	**TX10P**	**TX90P**	**DTR**
Hurst	0.8298	0.7133	0.5738	0.7149	0.9573	0.9305	0.6601	0.8092	0.8127

3.3. Correlation Analysis between Extreme Climate Indices and Teleconnection Patterns

3.3.1. Simple Correlation Analysis

There was a close relationship observed between extreme climate indices and teleconnection patterns in the Beijing–Tianjin–Hebei region (Figure 8). The results showed that PolarEA was significantly correlated with most indices such as RX1day, RX5day, R99P, and SDII in extreme precipitation indices and TNn, TXn, and TN90P in extreme temperature indices. The EA was significantly correlated with all extreme temperature indices, except DTR, TNn, and TXn. The AO had a significant correlation with extreme temperature indices, except DTR, TX90P, and TN90P. Both the EA and AO were significantly positively correlated with warm events, significantly negatively correlated with cold events, and had no significant correlation with the extreme precipitation indices. The EAWR had a significant correlation with extreme precipitation indices such as RX1day, RX5day, R99P, and SDII, but a weak correlation with extreme temperature indices. In addition, NAO was significantly correlated with CDD and TX10P, SCAND and WP were significantly correlated with CDD, while PNA and ENSO were not significantly correlated with the extreme climate index.

3.3.2. Wavelet Transform Coherence (WTC)

In terms of time and frequency space, four indices, CDD and R99p in the extreme precipitation indices, and FD0 and TXn in the extreme temperature indices, were selected as the dominant analysis indices. The effects of teleconnection patterns on extreme climate were further analyzed based on high Pearson coefficients.

The average wavelet coherence (AWC) and the percentage of the numbers of power (PNPS) that were significant at the 95% significance level for the WTC between extreme climate indices and teleconnection patterns in the Beijing–Tianjin–Hebei region are shown in Table 5. For the AWC of WTC, PNA and NAO were the dominant influencers of CDD; WP, EAWR, and PolarEA were the dominant influencers of R99p; PolarEA and PNA were the dominant influencers of TXn; and SCAND, WP, and EAWR were the dominant influencers of FD0. For the PASC of WTC, NAO and SCAND were the dominant constraints of CDD; WP, EAWR, and PolarEA were the dominant constraints of R99p; PNA and NAO were the dominant constraints of TXn; and SCAND and WP were the dominant constraints of FD0.

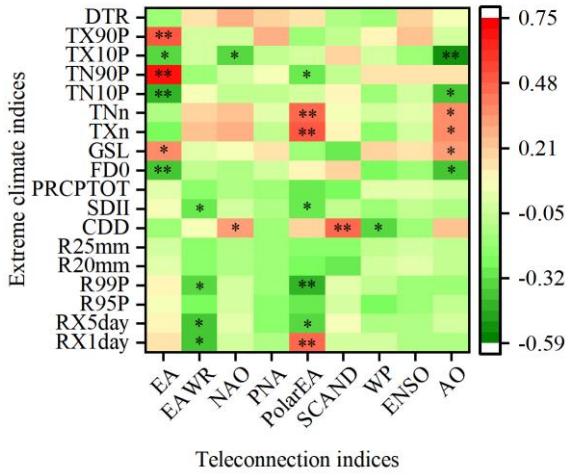

Figure 8. Correlation coefficient matrix of Beijing–Tianjin–Hebei extreme climate indices and teleconnection types (** indicates a significance level of 0.01; * indicates a significance level of 0.05).

Table 5. The average wavelet coherence (AWC) and the numbers of power (PNPS) of the wavelet transform coherence (WTC) between extreme climate indices and teleconnection patterns in the Beijing–Tianjin–Hebei region.

	CDD		R99p		TXn		FD0	
	AWC	**PASC(%)**	**AWC**	**PASC(%)**	**AWC**	**PASC(%)**	**AWC**	**PASC(%)**
EA	0.3380	1.10	0.3544	4.49	0.3234	0.51	0.4042	10.59
EAWR	0.3911	3.46	0.5493	24.41	0.3312	7.21	0.4431	6.91
NAO	0.4217	15.37	0.3486	6.62	0.3975	15.29	0.3714	7.35
PNA	0.4248	7.28	0.3417	10.96	0.4124	5.96	0.3641	11.32
PolarEA	0.3859	7.28	0.4711	23.97	0.4977	20.96	0.3529	4.19
SCAND	0.4851	12.43	0.4572	16.69	0.2998	1.32	0.5813	33.31
WP	0.3971	7.50	0.5595	34.56	0.3578	3.53	0.4820	14.49

The WTC shown in Figure 9 reveals the oscillatory relationship between the above-mentioned extreme climate indices and teleconnection patterns for the period 1980 to 2019. The thick black solid line inside Figure 9 indicates that the region passed the 95% significance test; the yellower the color of the wavelet coherence spectrum, the stronger the coherence between them. The arrows indicate the phase relationship, with a positive phase relationship to the right and a negative phase relationship to the left, and the upward arrow indicates that the teleconnection pattern was 1/4 period ahead of the extreme climate, while the opposite was 1/4 period behind. The phase relationship between the extreme climate indices and teleconnection patterns was consistent with the simple correlation results. The oscillation periods between these extreme climate indices and teleconnection patterns were mainly distributed around 4 years and 8 years, with both WP and EAWR leading R99P by 1/4 period in this time–frequency region. Most of the coherences showed continuous annual periodicity, with discontinuities only between CDD and NAO, SCAND, and between R99p and PolarEA.

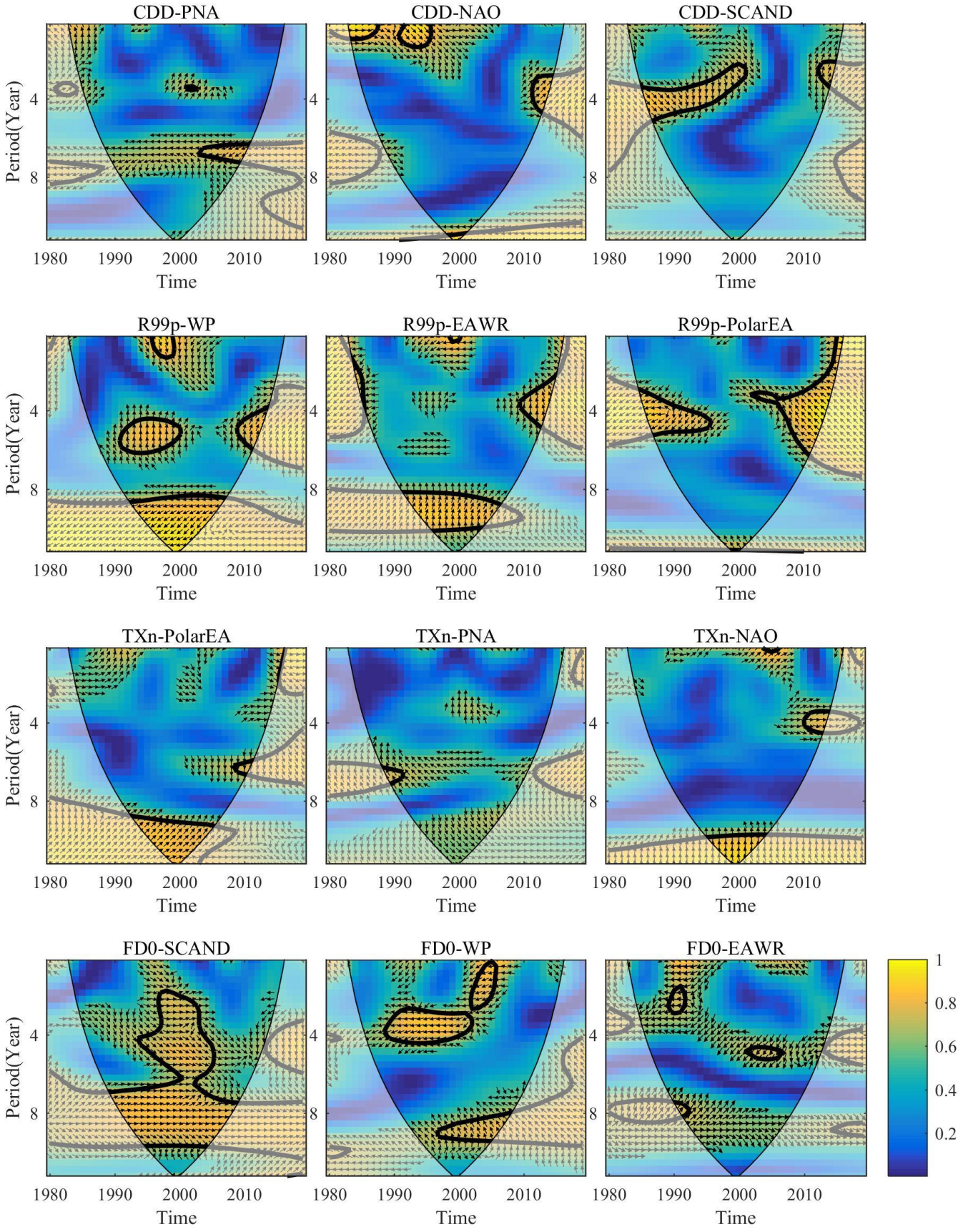

Figure 9. The WTC between extreme climate indices and teleconnection patterns in the Beijing–Tianjin–Hebei region.

3.3.3. Multiple Wavelet Coherence (MWC)

The explanatory effects of two-factor and three-factor combinations of teleconnection patterns on extreme climate using the MWC method are shown in Table 6. The explanatory power for climate extremes improves with the increase in the number of factors in the combinations. Among the combinations, the PolarEA–PNA and the addition of NAO contributed the least to explain TXn, with only a 0.66 increase in PASC. The factor combination of WP–EAWR–PolarEA best explained the P99p (AWC = 0.9311, PASC = 58.68%).

Table 6. The AWC and PASC of the multiple wavelet coherence (MWC) between extreme climate indices and teleconnection patterns in the Beijing–Tianjin–Hebei region.

	AWC	PASC(%)		AWC	PASC(%)
CDD–PNA–NAO	0.6993	16.32	TXn-PolarEA-PNA	0.7770	35.00
CDD–PNA–NAO–SCAND	0.8851	34.71	TXn-PolarEA-PNA-NAO	0.8966	35.66
R99P–WP–EAWR	0.7850	43.90	FD0-SCAND-WP	0.7527	17.94
R99P–WP–EAWR–PolarEA	0.9311	58.68	FD0-SCAND-WP-EAWR	0.8705	23.38

4. Discussion

4.1. Spatio–Temporal Variations in Extreme Climates

The Beijing–Tianjin–Hebei region has experienced frequent extreme climate events since the 1980s, with high-temperature weather, intensified persistent drought disasters, and a change in phenological seasons. These changes have affected the ecological environment of the region and gained the significant attention of the government and the scientific community [34]. Based on nine extreme precipitation indices and nine extreme temperature indices, we analyzed the spatiotemporal trends of extreme climate events in the Beijing–Tianjin–Hebei region for the period 1980 to 2019. Among all the extreme precipitation indices, only three (RX1day, RX5day, and R99p) showed a decreasing trend. The continuous dry days (CDD) showed an increasing trend. Among all the extreme temperature indices, high-temperature events such as GSL, TXn, TNn, TN90P, and TX90P showed an increasing trend, while low-temperature events such as FD0, TN90P, TX90P, and DTR showed a decreasing trend. All of these results indicate that the climate in the Beijing–Tianjin–Hebei region has tended to be warm and dry in recent decades, which is basically consistent with previous studies [7,35–38,55]. In addition, we found significant abrupt changes in extreme temperature events during 1988–1997, which were similar to the results of Zhang et al. [56] The reason for the slight differences may be that Zhang et al. [56] conducted their statistics based on meteorological stations. The climate in the Beijing–Tianjin–Hebei region is severely affected by global warming, and the gradual increase in temperature has led to an increase in the occurrence and frequency of extreme high-temperature events [34]. The results of the Hurst indices also show that in Beijing–Tianjin–Hebei, RX1day and R99P will exhibit an increase in the future, but R95P and CDD will decrease. Based on the findings, it can be suggested that high-temperature events will increase and low-temperature events will decrease. This indicates that the climate in the Beijing–Tianjin–Hebei region will further tend to be warm and humid in the future and the possibility of drought will decrease.

4.2. Influencing Factors of Extreme Climates

The change of extreme climate is restricted by many factors, among which the teleconnection patterns play the most important role [33]. Previous studies have shown that EA [57,58], EAWR [59,60], PolarEA [57,61,62], AO [63–65], NAO [38], ENSO 3.4 [38], SCAND [62,66,67], and PNA [68] influence the climate of the Beijing–Tianjin–Hebei region. In addition, there are also studies pointing out the influence of PNA [69], WP [69,70], and EAWR [70] on the atmosphere of Beijing–Tianjin–Hebei, which indirectly explains the influence of PNA, WP, and EAWR on the climate of Beijing–Tianjin–Hebei [9,71]. The results of this study show that extreme climate change in the Beijing–Tianjin–Hebei region is closely related to Northern Hemisphere teleconnection patterns. The PolarEA was

mainly negatively correlated with extreme precipitation events, negatively correlated with warm events, and positively correlated with cold events. The EA and AO were positively correlated with extreme warm events, while EAWR was negatively correlated with extreme precipitation events.

The PolarEA influenced the extreme climate changes in Eurasia by controlling the blocking high in the Ural Mountains and high-frequency transient waves. It had significant variation characteristics at different time scales and different seasons, and a great impact on blocking high and high-frequency transient waves, which have a significant impact on the extreme climate events in the Beijing–Tianjin–Hebei region [57,61]. Specifically, a negative POL pattern enhances water vapor transport to Beijing–Tianjin–Hebei, leading to increased precipitation in the region. Conversely, a positive POL pattern significantly reduces precipitation in Beijing–Tianjin–Hebei [62]. In addition, POL is conducive to the invasion of polar cold air mass into North China, leading to an increase in extreme cold events [72]. The EA influences the extreme climate of Beijing–Tianjin–Hebei through the combined effect of anticyclonic circulation anomalies located in Siberia and the Ural Mountains, with the circulation structure promoting the increase in temperature during positive anomalies and the opposite during negative anomalies [57,58]. The AO affects temperature changes in eastern China mainly by influencing the Siberian high, which is one of the most important circulation systems affecting China's climate, and usually weakens when AO strengthens [63–65]. In recent years, the rise of AO has weakened Siberian high pressure, leading to a decrease in the frequency of cold waves in the middle and high latitudes of China, which can be attributed to the high temperature and drought in the Beijing–Tianjin–Hebei region. The EAWR is closely related to the westerly belt over Eurasia. The westerly circulation is responsible for transporting water to the semi-arid regions of Central Asia, thus influencing the changes in extreme precipitation events in the Beijing–Tianjin–Hebei region [59]. When EAWR is enhanced, the westerly circulation weakens and extreme precipitation events in Beijing–Tianjin–Hebei decrease [73].

Teleconnection patterns do not work in isolation; their complex interactions also affect extreme climatic changes [13,26]. Through WCT and MWC analysis, this study found that with each additional factor combined, the AWC and PASC of wavelet coherence would increase. This indicates the explanatory power of teleconnection patterns for extreme climates, which is predicted to increase with the number of combined factors, consistent with previous research findings, such as Song et al. [38], Hu et al. [54], and Zhao et al. [74]. Different from Song et al. [38], the addition of teleconnection patterns in this study can significantly increase the PNSC value of MWC, which may be related to the difference in the selection of variables, indicating the complexity of the response mechanism of extreme climate to teleconnection patterns. Our results also show that the addition of NAO did not enhance explaining the change in TXn. This could be due to the great overlap in the region of significant influence between NAO and PolarEA–PNA in explaining the change in TXn.

4.3. Limitations and Uncertainties

In this study, only four typical extreme climate indices and the combinations of two to three factors were selected for coherence analysis. Since more factor combinations were not explored in depth, it is intended to further investigate influence patterns in follow-up work. In addition to teleconnection patterns, human activities such as urbanization are also an important cause of extreme climate changes [35,75]. Many studies have shown that human activities have aggravated the frequency and severity of extreme climate events [9,76–79]. Therefore, to predict the characteristics of extreme climate events in the Beijing–Tianjin–Hebei region more accurately, further in-depth and comprehensive analyses should be conducted on the combined effects of multiple teleconnections and the impacts of non-climatic factors such as human activities on extreme climate events.

5. Conclusions

The study used the daily temperature and precipitation data of the Beijing–Tianjin–Hebei meteorological stations for the period 1980 to 2019. The RClimDex model, trend analysis, probability density function, and wavelet coherence analysis were used to analyze the spatiotemporal variation characteristics of extreme climate events and their response mechanisms to teleconnection types in the Beijing–Tianjin–Hebei region. The conclusions were as follows:

(1) All the extreme precipitation indices, except RX1day, RX5day, and R99P showed an increasing trend. Among the extreme temperature indices, warm and cold events showed an increasing and decreasing trend, respectively. In terms of spatial patterns, except for SDII and R20mm, most of the stations showed a decreasing trend for extreme precipitation indices. Most of the stations showed an increasing trend in warm events, while a decreasing trend in cold events. Overall, the climate in the Beijing–Tianjin–Hebei region has tended to be warm and dry in recent decades.

(2) During 1980–2019, extreme rainfall events occurred more frequently, high-temperature events both increased in severity and frequency, and low-temperature events increased in frequency but decreased in severity. In the future, the trends of CDD in extreme precipitation indices will show strong discontinuities, and the extreme temperature indices will continue to follow the past 40 year trend.

(3) Correlation analysis showed that the teleconnection pattern was the main factor influencing extreme climate change. In addition, the analysis of WTC and MWC showed that the multi-factor combination greatly enhanced the explanatory power of the teleconnection pattern for extreme climate. It was observed that the explanatory power for extreme climate increased with the increase in the combination factors.

Author Contributions: Conceptualization, A.Z.; formal analysis, J.W.; data curation, J.W.; writing—original draft preparation, J.W.; writing—review and editing, A.Z. All authors have read and agreed to the published version of the manuscript.

Funding: This research was funded by the Natural Science Foundation of Hebei Province, grant number D2022402030.

Institutional Review Board Statement: Not applicable.

Informed Consent Statement: Not applicable.

Data Availability Statement: Not applicable.

Acknowledgments: The authors greatly acknowledge the National Meteorological Information Center (http://data.cma.cn/, accessed on 21 February 2022) and the National Marine Meteorological Service (http://www.noaa.gov/, accessed on 12 February 2022) for their free access to the datasets.

Conflicts of Interest: The authors declare no conflict of interest.

References

1. Liu, X.; Zhu, X.; Pan, Y.; Li, S.; Liu, Y.; Ma, Y. Agricultural drought monitoring: Progress, challenges, and prospects. *J. Geogr. Sci.* **2016**, *26*, 750–767. [CrossRef]
2. Gills, B.; Morgan, J. Global climate emergency: After COP24, climate science, urgency, and the threat to humanity. *Globalizations* **2020**, *17*, 885–902. [CrossRef]
3. Richards, C.; Lupton, R.; Allwood, J.M. Re-framing the threat of global warming: An empirical causal loop diagram of climate change, food insecurity and societal collapse. *Clim. Chang.* **2021**, *164*, 49. [CrossRef]
4. Xue, X.; Wang, T.; Guo, J.; Yang, Y.; Peng, F.; Liu, L. Impact of global warming on drought in China. *Sci. Cold Arid. Reg.* **2012**, *4*, 201–210.
5. Lloret, F.; Escudero, A.; Iriondo, J.M.; Martínez-Vilalta, J.; Valladares, F. Extreme climatic events and vegetation: The role of stabilizing processes. *Glob. Chang. Biol.* **2012**, *18*, 797–805. [CrossRef]
6. Horton, D.E.; Johnson, N.C.; Singh, D.; Swain, D.L.; Rajaratnam, B.; Diffenbaugh, N.S. Contribution of changes in atmospheric circulation patterns to extreme temperature trends. *Nature* **2015**, *522*, 465–469. [CrossRef]
7. Wu, J.; Han, Z.; Xu, Y.; Zhou, B.; Gao, X. Changes in extreme climate events in China under 1.5 C–4 C global warming targets: Projections using an ensemble of regional climate model simulations. *J. Geophys. Res. Atmos.* **2020**, *125*, e2019JD031057. [CrossRef]

8. Ebi, K.L.; Vanos, J.; Baldwin, J.W.; Bell, J.E.; Hondula, D.M.; Errett, N.A.; Hayes, K.; Reid, C.E.; Saha, S.; Spector, J. Extreme weather and climate change: Population health and health system implications. *Annu. Rev. Public Health* **2021**, *42*, 293. [CrossRef]
9. Masson-Delmotte, V.; Zhai, P.; Pirani, A.; Connors, S.L.; Péan, C.; Berger, S.; Caud, N.; Chen, Y.; Goldfarb, L.; Gomis, M. *Climate Change 2021: The Physical Science Basis. Contribution of Working Group I to the Sixth Assessment Report of the Intergovernmental Panel on Climate Change*; Cambridge University Press: Cambridge, UK; New York, NY, USA, 2021.
10. Alexander, L.V.; Zhang, X.; Peterson, T.C.; Caesar, J.; Gleason, B.; Klein Tank, A.; Haylock, M.; Collins, D.; Trewin, B.; Rahimzadeh, F. Global observed changes in daily climate extremes of temperature and precipitation. *J. Geophys. Res. Atmos.* **2006**, *111*, 1042–1063. [CrossRef]
11. Diffenbaugh, N.S.; Singh, D.; Mankin, J.S.; Horton, D.E.; Swain, D.L.; Touma, D.; Charland, A.; Liu, Y.; Haugen, M.; Tsiang, M. Quantifying the influence of global warming on unprecedented extreme climate events. *Proc. Natl. Acad. Sci. USA* **2017**, *114*, 4881–4886. [CrossRef]
12. Yuan, M.; Zhu, Q.; Zhang, J.; Liu, J.; Chen, H.; Peng, C.; Li, P.; Li, M.; Wang, M.; Zhao, P. Global response of terrestrial gross primary productivity to climate extremes. *Sci. Total Environ.* **2021**, *750*, 142337. [CrossRef] [PubMed]
13. Diatta, S.; Diedhiou, C.W.; Dione, D.M.; Sambou, S. Spatial variation and trend of extreme precipitation in west africa and teleconnections with remote indices. *Atmosphere* **2020**, *11*, 999. [CrossRef]
14. Odoulami, R.C.; Akinsanola, A. Recent assessment of West African summer monsoon daily rainfall trends. *Weather* **2018**, *73*, 283–287. [CrossRef]
15. Tangang, F.; Juneng, L.; Aldrian, E. Observed changes in extreme temperature and precipitation over Indonesia. *Int. J. Climatol.* **2017**, *37*, 1979–1997.
16. Alexander, L.V.; Arblaster, J.M. Historical and projected trends in temperature and precipitation extremes in Australia in observations and CMIP5. *Weather. Clim. Extrem.* **2017**, *15*, 34–56. [CrossRef]
17. Han, J.; Du, H.; Wu, Z.; He, H.S. Changes in extreme precipitation over dry and wet regions of China during 1961–2014. *J. Geophys. Res. Atmos.* **2019**, *124*, 5847–5859. [CrossRef]
18. Guo, E.; Zhang, J.; Wang, Y.; Quan, L.; Zhang, R.; Zhang, F.; Zhou, M. Spatiotemporal variations of extreme climate events in Northeast China during 1960–2014. *Ecol. Indic.* **2019**, *96*, 669–683. [CrossRef]
19. Rousta, I.; Doostkamian, M.; Taherian, A.M.; Haghighi, E.; Ghafarian Malamiri, H.R.; Ólafsson, H. Investigation of the spatio-temporal variations in atmosphere thickness pattern of Iran and the Middle East with special focus on precipitation in Iran. *Climate* **2017**, *5*, 82. [CrossRef]
20. Rousta, I.; Soltani, M.; Zhou, W.; Cheung, H.H. Analysis of extreme precipitation events over central plateau of Iran. *Am. J. Clim. Chang.* **2016**, *5*, 297–313. [CrossRef]
21. Rousta, I.; Karampour, M.; Doostkamian, M.; Olafsson, H.; Zhang, H.; Mushore, T.D.; Karimvandi, A.S.; Vargas, E.R.M. Synoptic-dynamic analysis of extreme precipitation in Karoun River Basin, Iran. *Arab. J. Geosci.* **2020**, *13*, 83. [CrossRef]
22. Kosaka, Y.; Xie, S.-P. Recent global-warming hiatus tied to equatorial Pacific surface cooling. *Nature* **2013**, *501*, 403–407. [CrossRef] [PubMed]
23. Shi, N.; Zhang, D.; Wang, Y.; Tajie, S. Subseasonal influences of teleconnection patterns on the boreal wintertime surface air temperature over southern China as revealed from three reanalysis datasets. *Atmosphere* **2019**, *10*, 514. [CrossRef]
24. Yang, J.; Chen, H.; Song, Y.; Zhu, S.; Zhou, B.; Zhang, J. Atmospheric circumglobal teleconnection triggered by spring land thermal anomalies over West Asia and its possible impacts on early summer climate over northern China. *J. Clim.* **2021**, *34*, 5999–6021. [CrossRef]
25. Yuan, F.; Liu, J.; Berndtsson, R.; Hao, Z.; Cao, Q.; Wang, H.; Du, Y.; An, D. Changes in precipitation extremes over the source region of the Yellow River and its relationship with teleconnection patterns. *Water* **2020**, *12*, 978. [CrossRef]
26. Yang, Y.; Gan, T.Y.; Tan, X. Spatiotemporal changes in precipitation extremes over Canada and their teleconnections to large-scale climate patterns. *J. Hydrometeorol.* **2019**, *20*, 275–296. [CrossRef]
27. Xi, Y.; Miao, C.; Wu, J.; Duan, Q.; Lei, X.; Li, H. Spatiotemporal Changes in Extreme Temperature and Precipitation Events in the Three-Rivers Headwater Region, China. *J. Geophys. Res. Atmos.* **2018**, *123*, 5827–5844. [CrossRef]
28. Mubarrok, S.; Jang, C.J. Annual Maximum Precipitation in Indonesia and Its Association to Climate Teleconnection Patterns: An Extreme Value Analysis. *SOLA* **2022**, *18*, 187–192. [CrossRef]
29. Craig, P.M.; Allan, R.P. The role of teleconnection patterns in the variability and trends of growing season indices across Europe. *Int. J. Climatol.* **2022**, *42*, 1072–1091. [CrossRef]
30. Qianrong, M.; Rui, H.; Yongping, W.; Jie, Z.; Rong, Z.; Guoling, F. Variations in July extreme precipitation in Henan Province and the related mechanisms. *Int. J. Climatol.* **2022**. [CrossRef]
31. Zhou, Y.; Ruan, G.; Xu, C.Y.; Xiong, L.; Jain, S.K.; Li, L. Detection and attribution of Norwegian annual precipitation variability related to teleconnections. *Earth Space Sci.* **2022**, *9*, e2021EA001857. [CrossRef]
32. Syed, F.; Adnan, S.; Zamreeq, A.; Ghulam, A. Identification of droughts over Saudi Arabia and global teleconnections. *Nat. Hazards* **2022**, *112*, 2717–2737. [CrossRef]
33. Cheng, Q.; Zhong, F.; Wang, P. Potential linkages of extreme climate events with vegetation and large-scale circulation indices in an endorheic river basin in northwest China. *Atmos. Res.* **2021**, *247*, 105256. [CrossRef]
34. Jiang, R.; Liang, J.; Zhao, Y.; Wang, H.; Xie, J.; Lu, X.; Li, F. Assessment of vegetation growth and drought conditions using satellite-based vegetation health indices in Jing-Jin-Ji region of China. *Sci. Rep.* **2021**, *11*, 13775. [CrossRef]

35. Zhao, N.; Jiao, Y.; Ma, T.; Zhao, M.; Fan, Z.; Yin, X.; Liu, Y.; Yue, T. Estimating the effect of urbanization on extreme climate events in the Beijing-Tianjin-Hebei region, China. *Sci. Total Environ.* **2019**, *688*, 1005–1015. [CrossRef]
36. Wang, Y.; Ren, Y.; Song, L.; Xiang, Y. Responses of extreme high temperatures to urbanization in the Beijing–Tianjin–Hebei urban agglomeration in the context of a changing climate. *Meteorol. Appl.* **2021**, *28*, e2024. [CrossRef]
37. Tong, R.; Sun, W.; Han, Q.; Yu, J.; Tian, Z. Spatial and temporal variations in extreme precipitation and temperature events in the Beijing–Tianjin–Hebei region of China over the past six decades. *Sustainability* **2020**, *12*, 1415. [CrossRef]
38. Song, X.; Zhang, C.; Zhang, J.; Zou, X.; Mo, Y.; Tian, Y. Potential linkages of precipitation extremes in Beijing-Tianjin-Hebei region, China, with large-scale climate patterns using wavelet-based approaches. *Theor. Appl. Climatol.* **2020**, *141*, 1251–1269. [CrossRef]
39. Wang, H.; Zhang, B.; Liu, Y.; Liu, Y.; Xu, S.; Deng, Y.; Zhao, Y.; Chen, Y.; Hong, S. Multi-dimensional analysis of urban expansion patterns and their driving forces based on the center of gravity-GTWR model: A case study of the Beijing-Tianjin-Hebei urban agglomeration. *Acta Geogr. Sin.* **2018**, *73*, 1076–1092.
40. Saleem, M.U.; Ahmed, S.R. Missing data imputations for upper air temperature at 24 standard pressure levels over pakistan collected from Aqua satellite. *J. Data Anal. Inf. Process.* **2016**, *4*, 132–146. [CrossRef]
41. Ferrari, G.T.; Ozaki, V. Missing data imputation of climate datasets: Implications to modeling extreme drought events. *Rev. Bras. De Meteorol.* **2014**, *29*, 21–28. [CrossRef]
42. Zhu, Z.; Piao, S.; Xu, Y.; Bastos, A.; Ciais, P.; Peng, S. The effects of teleconnections on carbon fluxes of global terrestrial ecosystems. *Geophys. Res. Lett.* **2017**, *44*, 3209–3218. [CrossRef]
43. Zhang, X.; Yang, F. RClimDex (1.0) user manual. *Clim. Res. Branch Environ. Can.* **2004**, *22*. Available online: http://www.acmad.net/rcc/procedure/RClimDexUserManual.pdf (accessed on 23 November 2022).
44. Wold, S.; Esbensen, K.; Geladi, P. Principal component analysis. *Chemom. Intell. Lab. Syst.* **1987**, *2*, 37–52. [CrossRef]
45. Shlens, J. A tutorial on principal component analysis. *arXiv* **2014**, arXiv:1404.1100.
46. Lever, J.; Krzywinski, M.; Altman, N. Points of significance: Principal component analysis. *Nat. Methods* **2017**, *14*, 641–643. [CrossRef]
47. Gocic, M.; Trajkovic, S. Analysis of changes in meteorological variables using Mann-Kendall and Sen's slope estimator statistical tests in Serbia. *Glob. Planet. Chang.* **2013**, *100*, 172–182. [CrossRef]
48. Yu, Y.-S.; Zou, S.; Whittemore, D. Non-parametric trend analysis of water quality data of rivers in Kansas. *J. Hydrol.* **1993**, *150*, 61–80. [CrossRef]
49. Pettitt, A.N. A non-parametric approach to the change-point problem. *J. R. Stat. Soc. Ser. C (Appl. Stat.)* **1979**, *28*, 126–135. [CrossRef]
50. Hurst, H.E. Long-term storage capacity of reservoirs. *Trans. Am. Soc. Civ. Eng.* **1951**, *116*, 770–799. [CrossRef]
51. Grinsted, A.; Moore, J.C.; Jevrejeva, S. Application of the cross wavelet transform and wavelet coherence to geophysical time series. *Nonlinear Process. Geophys.* **2004**, *11*, 561–566. [CrossRef]
52. Su, L.; Miao, C.; Duan, Q.; Lei, X.; Li, H. Multiple-wavelet coherence of world's large rivers with meteorological factors and ocean signals. *J. Geophys. Res. Atmos.* **2019**, *124*, 4932–4954. [CrossRef]
53. Torrence, C.; Compo, G.P. A practical guide to wavelet analysis. *Bull. Am. Meteorol. Soc.* **1998**, *79*, 61–78. [CrossRef]
54. Hu, W.; Si, B.C. Multiple wavelet coherence for untangling scale-specific and localized multivariate relationships in geosciences. *Hydrol. Earth Syst. Sci.* **2016**, *20*, 3183–3191. [CrossRef]
55. Xu, C.; Lu, C.; Sun, Q. Impact of climate change on irrigation water requirement of wheat growth–A case study of the Beijing-Tianjin-Hebei region in China. *Urban Clim.* **2021**, *39*, 100971. [CrossRef]
56. Zhang, Y.; Huang, G.; Wang, X.; Liu, Z. Observed changes in temperature extremes for the Beijing–Tianjin–Hebei region of China. *Meteorol. Appl.* **2017**, *24*, 74–83. [CrossRef]
57. Gao, N.; Bueh, C.; Xie, Z.; Gong, Y. A novel identification of the Polar/Eurasia pattern and its weather impact in May. *J. Meteorol. Res.* **2019**, *33*, 810–825. [CrossRef]
58. Fan, S.; Yang, X. Arctic and East Asia winter climate variations associated with the eastern Atlantic pattern. *J. Clim.* **2017**, *30*, 573–583. [CrossRef]
59. Gao, T.; Yu, J.-Y.; Paek, H. Impacts of four northern-hemisphere teleconnection patterns on atmospheric circulations over Eurasia and the Pacific. *Theor. Appl. Climatol.* **2017**, *129*, 815–831. [CrossRef]
60. Chen, S.; Guo, J.; Song, L.; Cohen, J.B.; Wang, Y. Temporal disparity of the atmospheric systems contributing to interannual variation of wintertime haze pollution in the North China Plain. *Int. J. Climatol.* **2020**, *40*, 128–144. [CrossRef]
61. Bueh, C.; Li, Y.; Lin, D.; Lian, Y. Interannual variability of summer rainfall over the northern part of China and the related circulation features. *J. Meteorol. Res.* **2016**, *30*, 615–630. [CrossRef]
62. Lin, Z. Intercomparison of the impacts of four summer teleconnections over Eurasia on East Asian rainfall. *Adv. Atmos. Sci.* **2014**, *31*, 1366–1376. [CrossRef]
63. Thompson, D.W.; Wallace, J.M. The Arctic Oscillation signature in the wintertime geopotential height and temperature fields. *Geophys. Res. Lett.* **1998**, *25*, 1297–1300. [CrossRef]
64. Thompson, D.W.; Wallace, J.M.; Hegerl, G.C. Annular modes in the extratropical circulation. Part II: Trends. *J. Clim.* **2000**, *13*, 1018–1036. [CrossRef]
65. Bingyi, W.; Jia, W. Possible impacts of winter Arctic Oscillation on Siberian high, the East Asian winter monsoon and sea–ice extent. *Adv. Atmos. Sci.* **2002**, *19*, 297–320. [CrossRef]

66. Bueh, C.; Shi, N.; Ji, L. Maintenance mechanism of the Scandinavian pattern in its positive phase during 2000/2001 winter and its influence on the weather over the northern part of China. *Plateau Meteorol.* **2008**, *27*, 76–83.
67. Liu, Y.; Liu, Y. The impact of the Scandinavian teleconnection pattern on late autumn rainfall in the western region of southwest China. *Clim. Environ. Res.* **2017**, *22*, 80–88. (In Chinese)
68. Lu, Q.; Rao, J.; Shi, C.; Guo, D.; Fu, G.; Wang, J.; Liang, Z. Possible influence of Sudden Stratospheric Warmings on the atmospheric environment in the Beijing-Tianjin-Hebei region. *Atmos. Chem. Phys. Discuss.* **2022**, *22*, 13087–13102. [CrossRef]
69. Zhang, Z.; Zhang, X.; Gong, D.; Kim, S.-J.; Mao, R.; Zhao, X. Possible influence of atmospheric circulations on winter haze pollution in the Beijing–Tianjin–Hebei region, northern China. *Atmos. Chem. Phys.* **2016**, *16*, 561–571. [CrossRef]
70. Yin, Z.; Wang, H.; Chen, H. Understanding severe winter haze events in the North China Plain in 2014: Roles of climate anomalies. *Atmos. Chem. Phys.* **2017**, *17*, 1641–1651. [CrossRef]
71. Shang, H.; Letu, H.; Pan, X.; Wang, Z.; Ma, R.; Liu, C.; Dai, T.; Li, S.; Chen, L.; Chen, C. Diurnal haze variations over the North China plain using measurements from Himawari-8/AHI. *Atmos. Environ.* **2019**, *210*, 100–109. [CrossRef]
72. Luo, Y.; Shi, J.; An, X.; Li, C. The combined impact of subtropical wave train and Polar− Eurasian teleconnection on the extreme cold event over North China in January 2021. *Clim. Dyn.* **2022**, 1–14. [CrossRef]
73. Irannezhad, M.; Chen, D.; Kløve, B. Interannual variations and trends in surface air temperature in Finland in relation to atmospheric circulation patterns, 1961–2011. *Int. J. Climatol.* **2015**, *35*, 3078–3092. [CrossRef]
74. Zhao, R.; Biswas, A.; Zhou, Y.; Zhou, Y.; Shi, Z.; Li, H. Identifying localized and scale-specific multivariate controls of soil organic matter variations using multiple wavelet coherence. *Sci. Total Environ.* **2018**, *643*, 548–558. [CrossRef] [PubMed]
75. Lin, L.; Gao, T.; Luo, M.; Ge, E.; Yang, Y.; Liu, Z.; Zhao, Y.; Ning, G. Contribution of urbanization to the changes in extreme climate events in urban agglomerations across China. *Sci. Total Environ.* **2020**, *744*, 140264. [CrossRef] [PubMed]
76. Zhu, X.; Zhang, Q.; Sun, P.; Singh, V.P.; Shi, P.; Song, C. Impact of urbanization on hourly precipitation in Beijing, China: Spatiotemporal patterns and causes. *Glob. Planet. Chang.* **2019**, *172*, 307–324. [CrossRef]
77. Gu, X.; Zhang, Q.; Li, J.; Singh, V.P.; Sun, P. Impact of urbanization on nonstationarity of annual and seasonal precipitation extremes in China. *J. Hydrol.* **2019**, *575*, 638–655. [CrossRef]
78. Zhang, P.; Ren, G.; Qin, Y.; Zhai, Y.; Zhai, T.; Tysa, S.K.; Xue, X.; Yang, G.; Sun, X. Urbanization effects on estimates of global trends in mean and extreme air temperature. *J. Clim.* **2021**, *34*, 1923–1945. [CrossRef]
79. Qian, Y.; Chakraborty, T.; Li, J.; Li, D.; He, C.; Sarangi, C.; Chen, F.; Yang, X.; Leung, L.R. Urbanization impact on regional climate and extreme weather: Current understanding, uncertainties, and future research directions. *Adv. Atmos. Sci.* **2022**, *39*, 819–860. [CrossRef]